PHYSICS OF FLUIDS **25**, 126601 (2013)

A new semi-analytical solution for inertial waves in a rectangular parallelepiped

S. Nurijanyan,[1,a)] O. Bokhove,[1,2,b)] and L. R. M. Maas[3,c)]
[1]*Department of Applied Mathematics, University of Twente, P.O. Box 217, 7500 AE, Enschede, The Netherlands*
[2]*School of Mathematics, University of Leeds, LS2 9JT Leeds, United Kingdom*
[3]*NIOZ Royal Netherlands Institute for Sea Research, P.O. Box 59, 1790 AB, Den Burg, The Netherlands*

(Received 13 November 2012; accepted 27 October 2013;
published online 13 December 2013)

A study of inertial gyroscopic waves in a rotating homogeneous fluid is undertaken both theoretically and numerically. A novel approach is presented to construct a semi-analytical solution of a linear three-dimensional fluid flow in a rotating rectangular parallelepiped bounded by solid walls. The three-dimensional solution is expanded in vertical modes to reduce the dynamics to the horizontal plane. On this horizontal plane, the two dimensional solution is constructed via superposition of "inertial" analogs of surface Poincaré and Kelvin waves reflecting from the walls. The infinite sum of inertial Poincaré waves has to cancel the normal flow of two inertial Kelvin waves near the boundaries. The wave system corresponding to every vertical mode results in an eigenvalue problem. Corresponding computations for rotationally modified surface gravity waves are in agreement with numerical values obtained by Taylor ["Tidal oscillations in gulfs and basins," Proc. London Math. Soc., Ser. 2 **XX**, 148–181 (1921)], Rao ["Free gravitational oscillations in rotating rectangular basins," J. Fluid Mech. **25**, 523–555 (1966)] and also, for inertial waves, by Maas ["On the amphidromic structure of inertial waves in a rectangular parallelepiped," Fluid Dyn. Res. **33**, 373–401 (2003)] upon truncation of an infinite matrix. The present approach enhances the currently available, structurally concise modal solution introduced by Maas. In contrast to Maas' approach, our solution does not have any convergence issues in the interior and does not suffer from Gibbs phenomenon at the boundaries. Additionally, an alternative finite element method is used to contrast these two semi-analytical solutions with a purely numerical one. The main differences are discussed for a particular example and one eigenfrequency. © *2013 AIP Publishing LLC*. [http://dx.doi.org/10.1063/1.4837576]

I. INTRODUCTION

Fluid phenomena on Earth involve rotation to a greater or lesser extent. There are flows in which rotation is an absolutely essential factor. Waves that are appearing in a closed rotating container filled with a homogeneous fluid became a subject of interest to the scientific community at the end of the 19th century and beginning of the 20th century. Taylor[1] derived and presented the first complete linear solutions (valid for any angular frequency) for free surface oscillations in a rotating rectangular parallelepiped. Before Taylor, Rayleigh[2] discussed the problem of the free tidal oscillations of a rectangular sea of uniform depth, when the vertical component of the Earth's rotation period is large compared with the periods of the oscillations. Later, the subject was studied by Proudman,[3,4] who also corrected some inaccuracies and errors in Rayleigh's works. A large

a)Electronic mail: s.nurijanyan@utwente.nl
b)Electronic mail: o.bokhove@leeds.ac.uk
c)Electronic mail: maas@nioz.nl

 © 2013 AIP Publishing LLC

amount of research has been focused on rotationally modified surface gravity waves as a major representative of the low-frequency waves in a homogeneous rotating fluid. In oceanography these are referred to as Poincaré and Kelvin waves, depending on whether the waves display a strictly sinusoidal or partially exponential spatial dependence (e.g., LeBlond and Mysak[5]). However, there is a class of inertial (gyroscopic) waves that are possible within the interior of homogeneous rotating fluids. Unlike the surface gravity waves, they have their maximum displacement in the interior of the domain, vanish at the free or solid surface, and are not affected by gravity. The frequencies of these waves are below the inertial frequency, $f = 2\Omega$, of the rotating domain, and they exist solely due to restoring Coriolis forces. No gravity effects are present in contrast to the case for surface gravity waves. Pure inertial waves were initially discovered theoretically by Kelvin[6] in a cylindrical domain. The axial spheroid was the next geometry where the hyperbolic equation governing the flow was solved by exactly satisfying the no-normal flow boundary conditions (Bryan[7]). Later, Maas[8] presented a semi-analytical structural solution in a rectangular parallelepiped with straight walls. Due to their symmetrical shape all three containers do not have any net focussing which inertial waves are otherwise prone to develop (Maas[9]). The axial spheroid has a symmetric structure, and thus compensates every reflected focussing wave with a reflected defocussing wave. In the case of an axial cylinder or a rectangular parallelepiped, the walls are either parallel or perpendicular to the rotation axis, therefore such walls possess a local reflectional symmetry. A simple tilt of one of the walls immediately results in symmetry breaking and hence in wave focussing and defocussing, such that due to dominance of the former, wave attractors may appear (e.g., Maas[9]).

All the above mentioned theoretical solutions have also been observed experimentally. Inertial waves were identified in a rotating axial cylinder by Fultz,[10] McEwan,[11] Manasseh,[12,13] Kobine,[14] in a slightly tilted free surface cylinder by Thompson,[15] in a sphere by Aldridge and Toomre,[16] in a tilted spheroid (tilt of its axis of rotation with respect to the axis of the cavity) by Malkus,[17] Vanyo *et al.*,[18] in a (truncated) cone by Beardsley,[19] in a rectangular parallelepiped by Bewley *et al.*,[20] Lamriben *et al.*,[21] Boisson *et al.*,[22] and in a trapezoid by Maas,[9] Manders and Maas.[23]

From the theoretical point of view, the solutions for the inertial waves presented by Maas[8] have a precise structure (revealed by use of the so-called Proudman-Rao method). The no-normal flow boundary conditions are satisfied exactly, by construction. Nevertheless, the solution is practically unusable, due to its poor convergence and Gibbs phenomenon at the boundaries, as shown in Sec. II. We substitute the solution back into the linear Euler equations governing the flow and calculate the residues. It appears that the residues of the momentum equations are not exactly zero, and moreover, their convergence to zero is very slow: with more than 200 Fourier modes, the residue still is only of order 10^{-1} of the maximum flow. The convergence of the residue is faster in the interior, in comparison to the boundaries, which is caused by the extra Gibbs phenomenon at the boundaries.

In this work, we present an enhanced solution for the free inertial waves of a rotating planar-rectangular parallelepiped, whose walls are parallel or perpendicular to the rotation axis. In Sec. II, we are presenting a detailed description of a new algorithm for the construction of this solution. As in Maas,[8] the three-dimensional solution is reduced to a two-dimensional one, by assuming a standing mode structure in the vertical direction. Thus, for every vertical mode, the problem reduces to the horizontal plane, where the techniques introduced by Taylor[1] for rotationally modified surface gravity waves are used. The solution is sought as a superposition of inertial Poincaré (IP) and inertial Kelvin (IK) waves in the rectangular parallelepiped, the strictly rotational internal counterparts of the rotationally modified external gravity waves (Maas[8]). Two IK waves are chosen as a "base" or particular solutions for the flow in the horizontal plane. The IK waves are assumed to have no motion in the x-direction ($u = 0$, $v = v(x, y)$), and thus they satisfy the no-normal flow boundary conditions at x-walls, $x =$ constant, automatically. IK waves grow exponentially in the along-wall, y-direction and are thus useful only when two opposite walls exist, excluding the unbounded growth that appears on infinite planes. Near the y-walls, the normal flow of these IK waves is compensated by addition of an infinite sum of IP waves. In other words, we are searching a superposition of IK and IP waves such that the flow governed by them will not be disturbed by the presence of the solid walls of the domain. The described algorithm (further called Taylor's method) results in an eigenvalue

problem for an infinite matrix, the finite truncation of which identifies the eigenfrequencies. The present algorithm has better convergence behaviour in the interior than the Proudman-Rao approach given by Maas:[8] the residues of the momentum equations are exactly zero (up to machine precision). Results are discussed by comparing solutions of one particular eigenfrequency.

Nonetheless, the convergence of the solution is slow near the boundaries. Therefore, in Sec. III, the problem is tackled purely from a numerical perspective by implementing a Finite Element (FEM) discretisation of the governing linear Euler equations on the horizontal plane. The calculated numerical eigenfrequencies exactly coincide with the results of the above discussed semi-analytical models. The differences between the numerical and the semi-analytical solutions are analysed for one particular eigenfrequency. The numerical results verify the new semi-analytical and FEM based methods. Conclusions are drawn in Sec. IV.

II. SEMI-ANALYTICAL INERTIAL WAVES IN A RECTANGULAR PARALLELEPIPED

A. 3D-to-2D reduction of governing equations

We consider a wave-tank (rectangular parallelepiped) with solid body rotation. The wave-tank has fixed solid walls, is filled with an incompressible, homogenous fluid, and is rotating about a vertical axis z_* with a constant angular velocity Ω_*, perpendicular to two of its side walls. Below, asterisks denote dimensional quantities. We closely follow the notation of Maas.[8] Small-amplitude monochromatic waves appearing in the homogenous fluid on a rotating f_*-plane ($f_* = 2\Omega_*$) are governed by the linearised, inviscid equations of motion

$$\frac{\partial u_*}{\partial t_*} - f_* v_* = -\frac{1}{\rho_*}\frac{\partial p_*}{\partial x_*}, \tag{1a}$$

$$\frac{\partial v_*}{\partial t_*} + f_* u_* = -\frac{1}{\rho_*}\frac{\partial p_*}{\partial y_*}, \tag{1b}$$

$$\frac{\partial w_*}{\partial t_*} = -\frac{1}{\rho_*}\frac{\partial p_*}{\partial z_*}, \tag{1c}$$

$$\frac{\partial u_*}{\partial x_*} + \frac{\partial v_*}{\partial y_*} + \frac{\partial w_*}{\partial z_*} = 0, \tag{1d}$$

where (u_*, v_*, w_*) are the three-dimensional velocity components in the corresponding Cartesian directions (x_*, y_*, z_*), p_* is the linearised reduced pressure and ρ_* is the density.

As in Maas,[8] we consider standing modes in the vertical direction to make w_* vanish at the rigid bottom $z_* = -H_*$ and top surface $z_* = 0$, i.e.,

$$w_* = \sum_{n=1}^{\infty} \frac{\partial \zeta_{n*}}{\partial t_*} \sin\frac{n\pi z_*}{H_*}, \tag{2a}$$

$$(u_*, v_*, p_*) = \sum_{n=1}^{\infty} (u_{n*}, v_{n*}, p_{n*}) \cos\frac{n\pi z_*}{H_*}, \tag{2b}$$

where subscript n refers to the nth vertical mode, and where we discarded the degenerate (geostrophic) mode with $n = 0$, and hence $w_* = 0$. The amplitude of the nth internal vertical elevation mode is denoted by ζ_{n*}. The presence of a solid wall at the top effectively eliminates the gravitational restoring forces and external gravity waves. Substitution of (2) into (1) modifies the governing equations in the following way:

$$\frac{\partial u_{n*}}{\partial t_*} - f_* v_{n*} = -H_{n*}\frac{\partial^3 \zeta_{n*}}{\partial x_* \partial t_*^2}, \tag{3a}$$

$$\frac{\partial v_{n*}}{\partial t_*} + f_* u_{n*} = -H_{n*} \frac{\partial^3 \zeta_{n*}}{\partial y_* \partial t_*^2}, \tag{3b}$$

$$\frac{\partial \zeta_{n*}}{\partial t_*} + H_{n*} \left(\frac{\partial u_*}{\partial x_*} + \frac{\partial v_*}{\partial y_*} \right) = 0, \tag{3c}$$

with $H_{n*} \equiv H_*/(n\pi)$ and $p_{n*} = \rho_* H_{n*}(\partial^2 \zeta_{n*}/\partial t_*^2)$. For a specific nth vertical mode, (3) can be non-dimensionalised with H_{n*} and f_*^{-1} as length and time scales as follows $(u, v) = (u_{n*}, v_{n*})/(H_{n*} f_*)$: $\zeta = \zeta_{n*}/H_{n*}$, $t = t_* f_*$ and $(x, y) = (x_*, y_*)/H_{n*}$. The dimensionless version of system (3) is

$$\frac{\partial u}{\partial t} - v = -\frac{\partial^3 \zeta}{\partial x \partial t^2}, \tag{4a}$$

$$\frac{\partial v}{\partial t} + u = -\frac{\partial^3 \zeta}{\partial y \partial t^2}, \tag{4b}$$

$$\frac{\partial \zeta}{\partial t} + \frac{\partial u}{\partial x} + \frac{\partial v}{\partial y} = 0. \tag{4c}$$

After substitution of $(u, v, \zeta) \propto \exp(-i\sigma t)$, system (4) becomes

$$(\Delta + \kappa^2)(u, v, \zeta) = 0, \tag{5}$$

where σ is the frequency of monochromatic waves, κ is defined by $\kappa^2 = 1/\sigma^2 - 1$, and the Laplacian is the following $\Delta = \partial_{xx} + \partial_{yy}$. Thus, the horizontal spatial structure of monochromatic waves is determined by the Helmholtz equation (5).

After choosing the ansatz (2), the three-dimensional problem for resolving the flow (u, v, w, p) transforms into a two-dimensional (u, v, ζ) problem in the two-dimensional container, defined in the region $0 \le x \le L$, $-Y \le y \le Y$. Therefore, we are looking for a solution which will satisfy (5) with no-normal flow boundary conditions at the four walls: $u = 0$ at $x = 0$ and $x = L$, and $v = 0$ at $y = -Y$ and $y = Y$. Recall that, because of the mode (n) dependent scaling, the boundary sizes, $L = n\pi L_*/H_*$ and $Y = n\pi Y_*/H_*$ also depend on this mode number.

As was already mentioned before, the solution provided via the Proudman-Rao method in Maas[8] satisfies the boundary conditions by construction, but suffers from poor convergence in the interior and Gibbs phenomenon at the boundaries. While some of the eigenfrequencies have indeed been obtained experimentally (Bewley *et al.*[20] and Lamriben *et al.*[21]) validating the precise shape of the corresponding eigenmodes has been more cumbersome (Boisson *et al.*[22]). This may of course be partially due to viscous boundary layers modifying the flow field near the boundaries, but may also partly be due to this convergence problem. The latter suggests that the development of a more precise method is desirable.

B. Taylor's method

We will present an alternative solution for determining the horizontal flow of the nth vertical mode in a rectangular parallelepiped. The method of Taylor is using a combination of results discussed in Maas[8] concerning inertial Poincaré waves and inertial Kelvin waves. Thus, the algorithm is applicable to semi-infinite as well as finite rectangular regions. The idea is as follows: we search for analytic solutions of the Helmholtz equations (5), which do not or only partially satisfy impermeability conditions at the boundary, but the superposition of which will meet the requirements at the boundaries. To construct the final solution, we use a combination of two IK and numerous IP waves defined in a finite meridional channel, available from Maas.[8] The IK wave solution of (4) for

a finite meridional channel is given by

$$u = 0, \tag{6a}$$

$$v = V\exp\left[-y + i\frac{x - L/2}{\sigma} - i\sigma t\right], \tag{6b}$$

$$\zeta = i\frac{v}{\sigma}. \tag{6c}$$

Obviously, the latter wave satisfies no-normal flow boundary condition only in the x-direction. Meanwhile, IP waves with quantised wave-numbers $\{k_m = m\pi/L\}, m \in \{1, 2, 3, ...\}$ are given by

$$u = v_m i k_m \frac{\sigma^3}{1-\sigma^2}\left[1 + \left(\frac{l_m}{\sigma k_m}\right)^2\right]\sin k_m x \exp i(l_m y - \sigma t), \tag{7a}$$

$$v = v_m\left(-l_m\sigma\cos k_m x + \frac{1}{k_m}\sin k_m x\right)\exp i(l_m y - \sigma t), \tag{7b}$$

$$\zeta = v_m(\cos k_m x + \frac{l_m}{\sigma k_m}\sin k_m x)\exp i(l_m y - \sigma t), \tag{7c}$$

where $\mathbf{k_m} = (k_m, l_m)$ is the two-dimensional wave number vector and $l_m = \pm(\sigma^{-2} - \sigma_m^{-2})^{1/2} \equiv -is_m$ is determined by frequency σ, wave number k_m and $\sigma_m = (1 + k_m^2)^{-1/2}$. These waves, however, do not satisfy the boundary conditions $v = 0$ at $y = \pm Y$, but by contrast do satisfy $u = 0$ at $x = 0, L$.

After dropping the common factor $\exp(-i\sigma t)$, a solution of the Helmholtz equation (5), expressed in terms of the meridional velocity v, is now supposed to consist of two IK waves that are trapped at the walls $y = \pm Y$, and of an infinite sum of channel IP waves, a finite number of which are free to propagate in the y-direction:

$$2v = v_+\exp(i(x - L/2)/\sigma - y) + v_-\exp(-i(x - L/2)/\sigma + y) + \sum_{m=-\infty, m\neq 0}^{+\infty} v_m(is_m\sigma\cos k_m x + \frac{1}{k_m}\sin k_m x)\exp(s_m y). \tag{8}$$

In view of the definition of σ_m, we find: $1 > \sigma_1 > \sigma_2 > \ldots$. Now, if our frequency σ lies in between two of these eigenfrequencies: $\sigma_M > \sigma > \sigma_{M+1}$, then the s_m are imaginary for all $m \leq M$, while they are real for $m > M$. This implies that the first M modes have real l_m. Since l_m represent wave numbers, this implies M propagating modes, while all modes having $m > M$ are trapped (real s_m). For negative m, we define $s_{-m} = -s_m$ and $k_{-m} = k_m$. Positive m refers either to energy propagation in positive y-direction, or trapping to $y = Y$ (depending on whether σ is larger or smaller than σ_m). Negative m refers to energy propagation in negative y-direction, or trapping to $y = -Y$. When we look for waves that are symmetric under reflection in the centre, $(x, y) \to (L - x, -y)$, the expression for v has to be invariant under this transformation. This requires $v_- = v_+ \equiv v_0$, $v_{2m} = -v_{-2m}$, $v_{2m+1} = v_{-(2m+1)}$. When we look for antisymmetric velocity fields v, these relations should reverse parity ($v_- = -v_+$, etc.). Consider now v-symmetric solutions and adopt a Cartesian coordinate frame ξ, y, whose origin is at the centre of the rectangle, where

$$\xi = \frac{\pi x}{L} - \frac{\pi}{2}. \tag{9}$$

The container is now restricted to $\xi \in [-\pi/2, \pi/2]$. Then, with

$$\alpha \equiv \frac{L}{\pi\sigma}, \tag{10}$$

the v-velocity can be expressed

$$v = \cosh y \cos\alpha\xi - i \sinh y \sin\alpha\xi + \frac{L}{\pi}\sum_{m\ odd}^{\infty}(-1)^{\frac{m-1}{2}} v_m(-i\frac{s_m}{\alpha}\sin m\xi \sinh s_m y + \frac{1}{m}\cos m\xi \cosh s_m y) + \frac{L}{\pi}\sum_{m\ even}^{\infty}(-1)^{\frac{m}{2}} v_m(i\frac{s_m}{\alpha}\cos m\xi \cosh s_m y + \frac{1}{m}\sin m\xi \sinh s_m y), \tag{11}$$

where the amplitude v_0 has been arbitrarily set equal to one. Here and in the following all integers occurring in summations are strictly positive. Notice the point symmetry of (11) as it is invariant under the transformation $(\xi, y) \to (-\xi, -y)$. The IK waves (the first two terms in (11)) provide a coupling between the IP waves, but numbers α should be non-integer, as the IK-waves would otherwise be exactly annihilated by one of the IP-waves (having $s_m = 1$). Eigenfrequencies and amplitudes of each of the terms in (11) follow by rewriting this expression and by application of the boundary condition at $y = \pm Y$.

The IK waves, possessing non-integer α, yield only the cosine of even and the sine of odd multiples of ξ in their Fourier representations, as in the case of reflecting Kelvin waves (Taylor[1]):

$$\cos\alpha\xi = \frac{4\alpha}{\pi}\sin\left(\frac{\alpha\pi}{2}\right)\left[\frac{1}{2\alpha^2} + \sum_{m\ even}\frac{(-1)^{\frac{m}{2}}}{\alpha^2 - m^2}\cos m\xi\right], \tag{12a}$$

$$\sin\alpha\xi = \frac{-4\alpha}{\pi}\cos\left(\frac{\alpha\pi}{2}\right)\sum_{m\ odd}\frac{(-1)^{\frac{m-1}{2}}}{\alpha^2 - m^2}\sin m\xi. \tag{12b}$$

These are, therefore, unable to match the cosine of odd and sine of even multiples of ξ, also occurring in (11). Now, we directly expand the terms $\cos\alpha\xi$ and $\sin\alpha\xi$ in (11) using (12) in cosine of even and sine of odd multiples of ξ, respectively, and require the coefficients of each of the trigonometric terms to vanish separately at $y = Y$. The same conditions are obtained by application of the boundary condition at the opposing boundary $y = -Y$. However, this direct approach yields an unwieldy matrix equation. Probably for this reason, Taylor extended (12a) with odd and (12b) with even multiplies ξ. The cosine expansion in (12a), for instance, is extended with $\cos s\xi$ (s odd), while each such term is counterbalanced by subtracting its even Fourier expansion (in another application of (12a) to odd integers such that in effects zeroes are added). Each such odd multiple and its counterbalancing Fourier expansion has an undetermined magnitude β_s (s odd). For the sine expansion similar terms are added yielding undetermined magnitude γ_s (s even). These undetermined magnitudes β_s and γ_s can be obtained from the requirement that the total velocity field v vanishes at $y = \pm Y$. The total velocity at $y = Y$ reads

$$v(\xi, Y) = \frac{4\alpha}{\pi}\cosh Y \sin\left(\frac{\alpha\pi}{2}\right)\left[\frac{1}{2\alpha^2} + \sum_{m\ even}^{\infty}\frac{(-1)^{\frac{m}{2}}}{\alpha^2 - m^2}\cos m\xi + \sum_{s\ odd}^{\infty}\beta_s\left((-1)^{\frac{s-1}{2}}\frac{\pi}{4s}\cos s\xi - \left(\frac{1}{2s^2} + \sum_{j\ even}^{\infty}\frac{(-1)^{\frac{j}{2}}}{s^2 - j^2}\cos j\xi\right)\right)\right] + i\frac{4\alpha}{\pi}\sinh Y \cos\left(\frac{\alpha\pi}{2}\right)\left[\sum_{m\ odd}^{\infty}\frac{(-1)^{\frac{m-1}{2}}}{\alpha^2 - m^2}\sin m\xi + \sum_{s\ even}^{\infty}\gamma_s\left((-1)^{\frac{s}{2}}\frac{\pi}{4s}\sin s\xi + \sum_{j\ odd}^{\infty}\frac{(-1)^{\frac{j-1}{2}}}{s^2 - j^2}\sin j\xi\right)\right]$$

$$+\frac{L}{\pi}\sum_{m\ odd}^{\infty}(-1)^{\frac{m-1}{2}}v_m(-i\frac{s_m}{\alpha}\sin m\xi\sinh s_mY+\frac{1}{m}\cos m\xi\cosh s_mY)$$

$$+\frac{L}{\pi}\sum_{m\ even}^{\infty}(-1)^{\frac{m}{2}}v_m(i\frac{s_m}{\alpha}\cos m\xi\cosh s_mY+\frac{1}{m}\sin m\xi\sinh s_mY). \tag{13}$$

Vanishing of this expression requires the separate vanishing of the coefficients of $\cos m\xi$ or $\sin m\xi$. For m odd, vanishing of the coefficient of $\cos m\xi$ requires

$$v_m=-\frac{\alpha\pi}{L}\frac{\cosh Y}{\cosh s_mY}\sin\left(\frac{\alpha\pi}{2}\right)\beta_m. \tag{14}$$

On the other hand, vanishing of the coefficient of $\sin m\xi$ requires

$$v_m=\frac{4\alpha^2}{s_mL}\frac{\sinh Y}{\sinh s_mY}\cos\left(\frac{\alpha\pi}{2}\right)\left[\frac{1}{\alpha^2-m^2}-\sum_{s\ even}^{\infty}\frac{\gamma_s}{m^2-s^2}\right]. \tag{15}$$

The equality of these two expressions for v_m determines β_m in terms of γ_s,

$$\frac{1}{m^2-\alpha^2}+\sum_{s\ even}^{\infty}\frac{\gamma_s}{m^2-s^2}+\beta_m\lambda_m=0, \tag{16}$$

where

$$\lambda_m=-\frac{s_m\pi}{4\alpha}\coth Y\tan\left(\frac{\alpha\pi}{2}\right)\tanh(s_mY). \tag{17}$$

For m even, we similarly find that vanishing of the coefficient of $\sin m\xi$ requires

$$v_m=-i\frac{\alpha\pi}{L}\frac{\sinh Y}{\sinh s_mY}\cos\left(\frac{\alpha\pi}{2}\right)\gamma_m. \tag{18}$$

Dividing this by the expression for v_m obtained from vanishing of the coefficient of $\cos m\xi$ one finds

$$-\frac{1}{m^2-\alpha^2}+\sum_{s\ odd}^{\infty}\frac{\beta_s}{m^2-s^2}+\gamma_m\mu_m=0, \tag{19}$$

where

$$\mu_m=\frac{s_m\pi}{4\alpha}\tanh Y\cot\left(\frac{\alpha\pi}{2}\right)\coth(s_mY). \tag{20}$$

If we define $\mu_0=0$, (19) also includes, for $m=0$, the extra requirement that the constant term in (13) vanishes. Note that in the expressions for λ_m and μ_m, s_m occurs in product with either $\tanh s_my$ or $\coth s_my$. The replacement $s_m=il_m$ when $\sigma<\sigma_m$, and the property $\tanh iz=i\tanh z$ (for real z), therefore leaves these expressions real, regardless of whether s_m is real or imaginary, making a cumbersome sign-distinction (as in Taylor[1]) unnecessary. It also guarantees λ_m and μ_m (and therefore the eigenfrequencies) to be real. Interpreting each first term of (16) and (19) as multiplying a quantity $\gamma_0(=1)$, the set of equations forms a system of infinite matrix equations $Ac=0$, where A is as follows

$$A=\begin{pmatrix}\frac{1}{\alpha^2} & \frac{-1}{1^2} & 0 & \frac{-1}{3^2} & 0 & \dots\\ \frac{1}{1^2-\alpha^2} & \lambda_1 & \frac{1}{1^2-2^2} & 0 & \frac{1}{1^2-4^2} & \dots\\ \frac{-1}{2^2-\alpha^2} & \frac{1}{2^2-1^2} & \mu_2 & \frac{1}{2^2-3^2} & 0 & \dots\\ \frac{1}{3^2-\alpha^2} & 0 & \frac{1}{3^2-2^2} & \lambda_3 & \frac{1}{3^2-4^2} & \dots\\ \cdot & & & & & \\ \cdot & & & & & \\ \cdot & & & & & \end{pmatrix} \tag{21}$$

and column vector $c=(\gamma_0,\ \beta_1,\ \gamma_2,\ \beta_3,\ \dots)^T$, where superscript T means transpose. Matrix A is twice as big as the matrix obtained when directly expanding the terms in (11), alluded to above, but

is much simpler to handle. Apart from differences in the definitions of the diagonal terms λ_m and μ_m, together with the fact that our α is a function of frequency, (10), the matrix equation exactly conforms with Taylor's. Nontrivial solutions result only when its determinant vanishes, $detA = 0$, which (through α) can be regarded as an equation establishing eigenfrequencies σ. Amplitudes β_m (m is odd) and γ_m (m is even), for any particular σ_j, $j = 1, 2...$ can be determined by the inversion of the reduced matrix that can be obtained from (16) and (19), where we now exclude the first row, corresponding to $m = 0$, and bring the first column to the right of the equation, which can now be regarded as known. With these amplitudes, from (15) and (18), also the amplitudes v_m in the expansion of v, Eq. (11), are determined, and the solution is in essence complete. We also note that similar expressions can be obtained for antisymmetric solutions, where

$$\lambda_m = -\frac{s_m \pi}{4\alpha} \tanh Y \tan\left(\frac{\alpha\pi}{2}\right) \coth(s_m Y), \tag{22a}$$

$$\mu_m = \frac{s_m \pi}{4\alpha} \coth Y \cot\left(\frac{\alpha\pi}{2}\right) \tanh(s_m Y) \tag{22b}$$

and making similar replacements, $\sinh Y \Longleftrightarrow -\cosh Y$ and $\sinh s_m Y \Longleftrightarrow \cosh s_m Y$, in coefficients v_m and again, but with regards to the y-dependence, in fields u, v, and ζ.

For each eigenvalue and corresponding set of amplitudes v_m, the velocity and elevation fields are now determined. Hence, the u velocity component of infinite sum of IP waves (7), with their corresponding eigenvalue and set of amplitudes v_m, reads

$$u = \sum_{m\ odd}^{\infty} i(-1)^{\frac{m-1}{2}} v_m \left(\frac{\alpha}{m} - \frac{m}{\alpha}\right) \cos m\xi \cosh s_m y + \sum_{m\ even}^{\infty} i(-1)^{\frac{m}{2}} v_m \left(\frac{\alpha}{m} - \frac{m}{\alpha}\right) \sin m\xi \sinh s_m y. \tag{23}$$

The vertical elevation field then follows from the continuity equation

$$\begin{aligned}\zeta = -\sigma^{-1}\left(\frac{\partial u}{\partial x} + \frac{\partial v}{\partial y}\right) &= -i\sigma^{-1}(\pi L^{-1} u_\xi + v_y) = -\sigma^{-1}(i \sinh y \cos\alpha\xi + \cosh y \sin\alpha\xi) \\ &- \sum_{m\ odd}^{\infty} i(-1)^{\frac{m-1}{2}} v_m \left(\sin m\xi \cosh s_m y + \frac{i\alpha s_m}{m} \cos m\xi \sinh s_m y\right) \\ &+ \sum_{m\ even}^{\infty} i(-1)^{\frac{m}{2}} v_m \left(\cos m\xi \sinh s_m y - \frac{i\alpha s_m}{m} \sin m\xi \cosh s_m y\right).\end{aligned} \tag{24}$$

The eigenfrequencies are determined by truncating the infinite matrix to include just N rows and columns. Finding the roots of the resulting determinant numerically, and observing convergence of these roots upon increase of the number of rows, the set of eigenfrequencies σ_j, $j = 1, 2...$ is determined (approximately).

C. Comparison of two methods: Taylor's method vs. Proudman-Rao method

Next, this novel Taylor's method for a construction of semi-analytical solutions for the linearised Euler equations in a rectangular parallelepiped is tested and verified from a numerical perspective. First a few eigenfrequencies are determined in a given $[\pi \times 2\pi]$ rectangle, see Figure 1. Also, an independent verification is performed by comparing the latter eigenfrequencies to the frequencies for a $[2\pi \times \pi]$ rectangle in Figure 1. The eigenfrequency of the first symmetric mode is $\sigma_1^* = L/\pi\alpha_1 \approx 0.657$, which corresponds to the first root in Figure 1(a), at $\alpha_1 \approx 1.522$. The next two eigenfrequencies of symmetric velocity modes are $\sigma_2^* = L/\pi\alpha_1 \approx 0.477$, $\alpha_2 \approx 2.095$ and $\sigma_3^* = L/\pi\alpha_1 \approx 0.398$, $\alpha_3 \approx 2.513$. Numerical computations for the frequencies and modal structures are assessed for several antisymmetric and symmetric modes. The eigenfrequencies and eigenmodes computed in this manner for the rotationally modified surface gravity modes are in

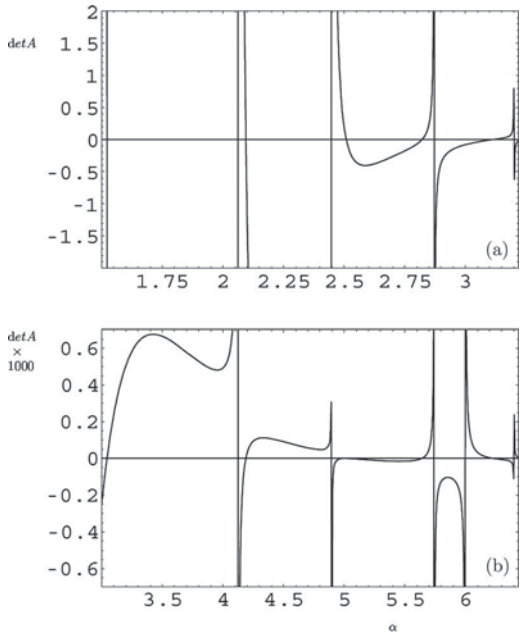

FIG. 1. (a) Det A as a function of α for $L = Y = \pi$ for a mode whose v-velocity is symmetric. Hence, $L \times 2Y = \pi \times 2\pi$. Intersections with the horizontal line give the eigenfrequencies. The vertical lines represent asymptotes whose intersections with the horizontal axis should be disregarded. (b) Det A (for clarity multiplied by 10^3) as a function of α for $L = 2\pi$, $Y = \pi/2$, which represents a $2\pi \times \pi$ rectangle. Since the present rectangle has a width L twice that in (a), and $\sigma = L/\pi\alpha$, eigenfrequencies will be the same when the zeroes are now found at α's twice that obtained in (a), which we verify by inspection.

agreement with numerical values obtained many years ago by Taylor[1] and later by Rao[24] and for the inertial modes with those computed in Maas.[8] It is also worth to mention that the Proudman-Rao method is much faster in converging to the modal eigenfrequencies compared to Taylor's method.

Furthermore, close agreement in the eigenfrequencies of the modes enables a comparison between corresponding velocity fields of semi-analytical inertial waves constructed by the present Taylor's method to the previously employed Proudman-Rao method. The semi-analytical solutions are assessed according to the following criteria: (i) satisfaction of governing equations, (ii) satisfaction of the boundary conditions, and (iii) speed of convergence. In both cases, solutions have the same standing mode structure in the vertical z-direction. Thus, the comparison is performed only on the horizontal plane. For a fair comparison in the calculations the same number of "basis functions" are used: IP waves in Taylor's method and Fourier modes in the Proudman-Rao method.

The comparison is performed on a $[2\pi \times \pi]$ domain for the highest mode $\sigma \approx 0.657$ of the antisymmetric velocity field. In Figure 2, the horizontal u and v velocity fields constructed via Taylor's method are presented. For the first comparison the constructed modal solutions were substituted into the linear Euler equations and the residues are calculated. Obviously, due to the construction, in both algorithms the continuity equation and third momentum equation are satisfied exactly. Thus, in Figures 3 and 4 only the residues for the u and v momentum equations are presented. It is apparent from Figure 3 that the Proudman-Rao method performs very poorly near the boundaries, which is explained by the Gibbs phenomenon. Also, the convergence is poor in the interior of the domain. By contrast, Figure 4 shows that in Taylor's method the rotating Euler equations are satisfied up to machine precision. The latter indicates that Taylor's method is preferable to Proudman-Rao, in this context. The differences between the constructed solutions are given in Figure 5. According to Figure 5, the main differences between the solutions are near the boundaries (y-wall for the u-component and x-wall for the v-component of the velocity). Near these boundaries the Proudman-Rao method suffers

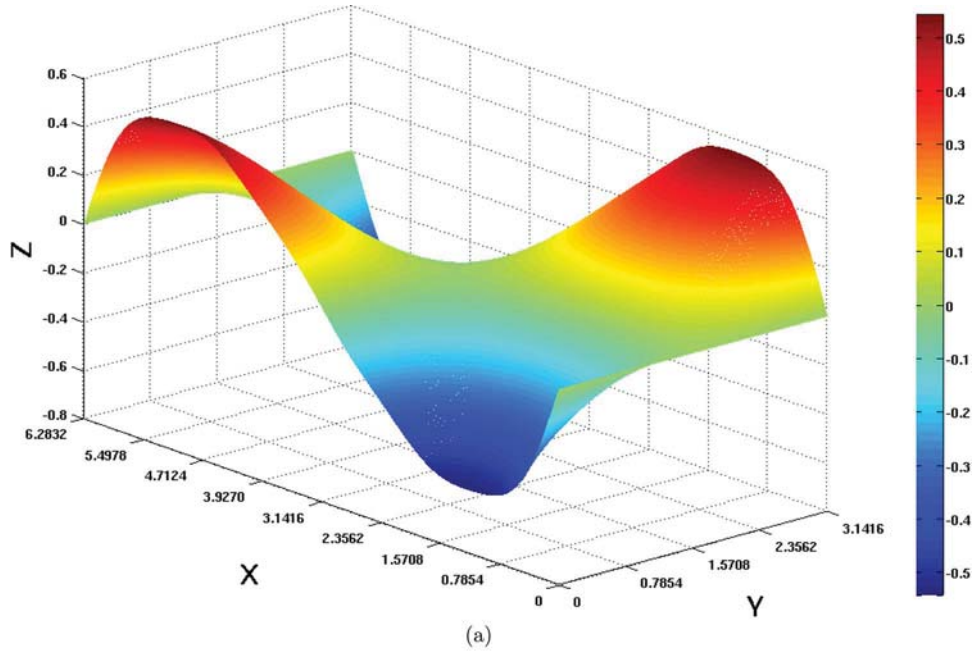

(a)

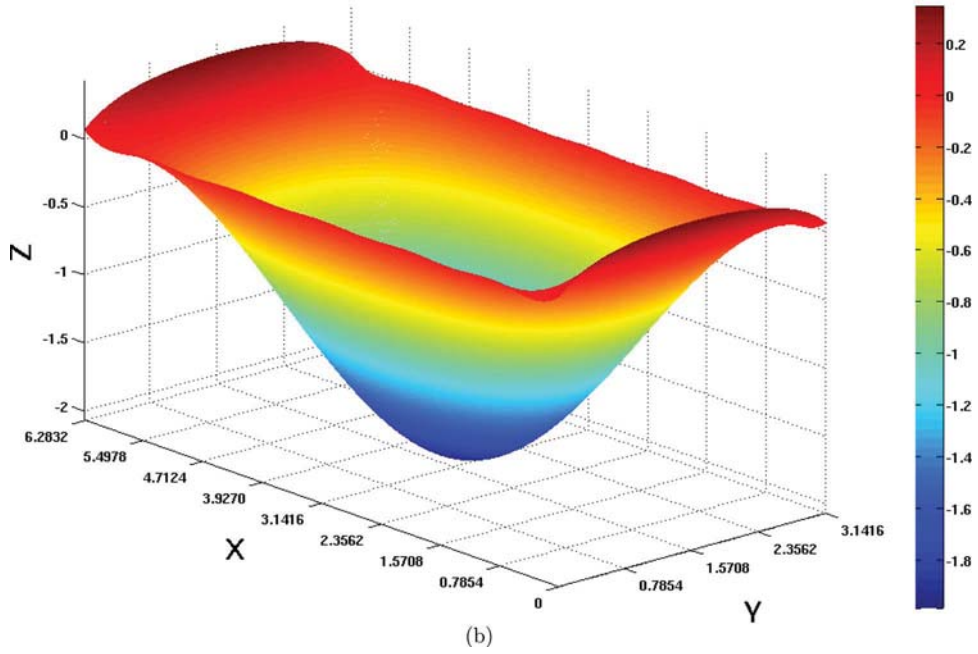

(b)

FIG. 2. Antisymmetric horizontal velocity fields on the $x - y$ plane for mode $\sigma \approx 0.657$ constructed via Taylor's method, (a) and (b) subfigures are $u(x, y)$ and $v(x, y)$, respectively. The domain is rotating anti-clockwise and 20 IP waves were used. (a) u profile; (b) v profile.

from a Gibbs phenomenon. In spite of its advantages, Taylor's method still has its flaws. The essence of the method is in "filling" the solution with numerous IP-waves, to compensate the IK-waves motion near the boundaries in order to satisfy the no-normal flow boundary conditions. Thus, the more IP-waves are taken, the less no-normal flow will be registered near the appropriate boundaries. As can be noticed from Figure 2, the convergence is poor: non-zero flow is present near the x-boundary for the v-component of the velocity field and similarly near the y-boundary for the u-component. The

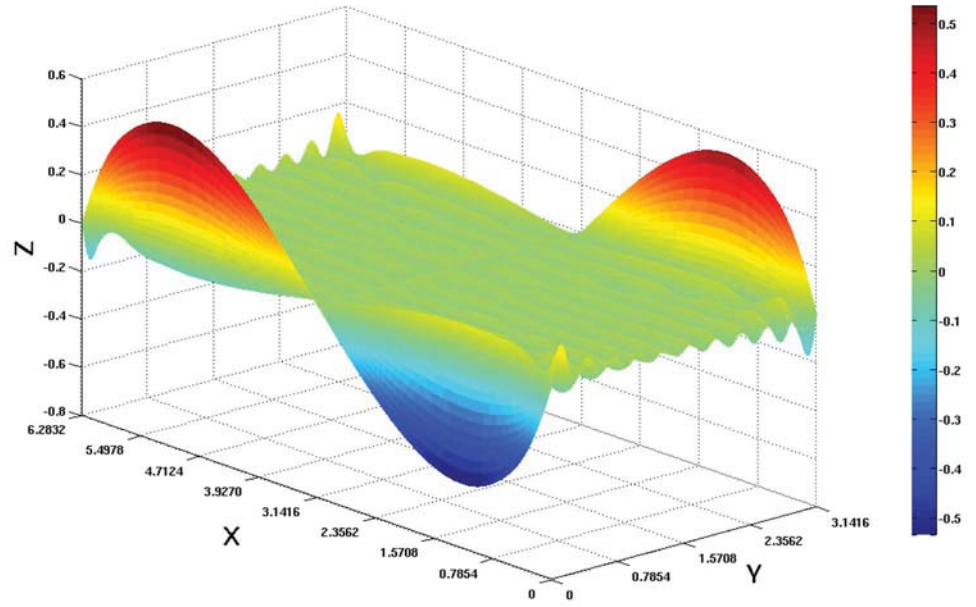

(a)

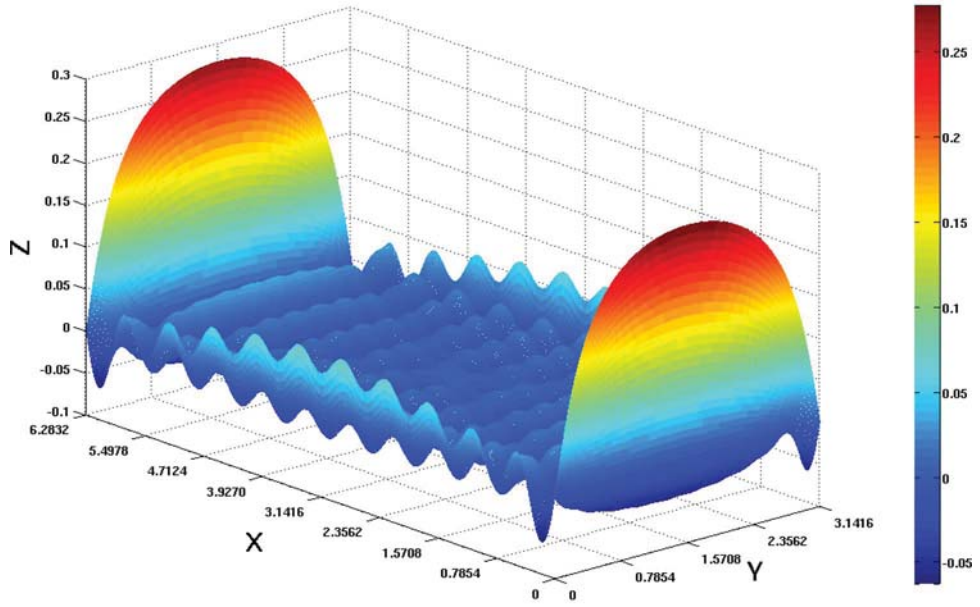

(b)

FIG. 3. Antisymmetric horizontal velocity fields in the x–y plane for a mode with frequency sigma $\sigma \approx 0.657$ were substituted in the linearised Euler equations. (a) and (b) subfigures are the residues for velocities u and v in their respective momentum equations, as produced by the Proudman-Rao method.

nature of the convergence near the boundaries can be observed more closely in Figure 6. It shows that when the number of IP waves exceeds 100, the curve nearly stops decreasing. The latter suggests that despite the satisfaction of the Euler equations up to machine precision, the velocities constructed by Taylor's method, are not satisfying the boundary conditions exactly. Therefore, Taylor's method fails the second comparison test, namely, satisfaction of the boundary conditions; whereas the satisfaction of the boundary conditions in the Proudman-Rao method was embedded in the construction.

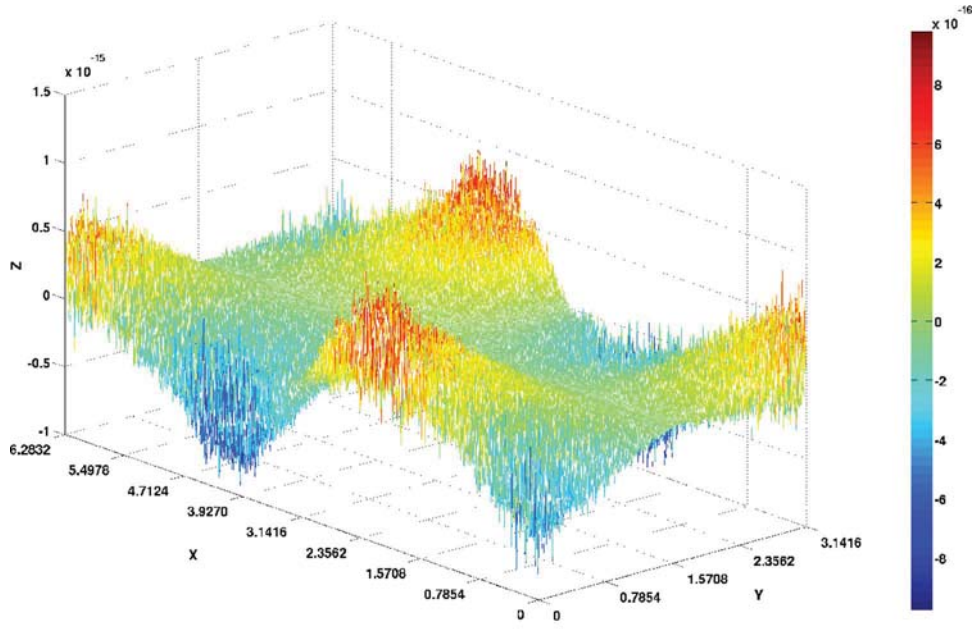

(a)

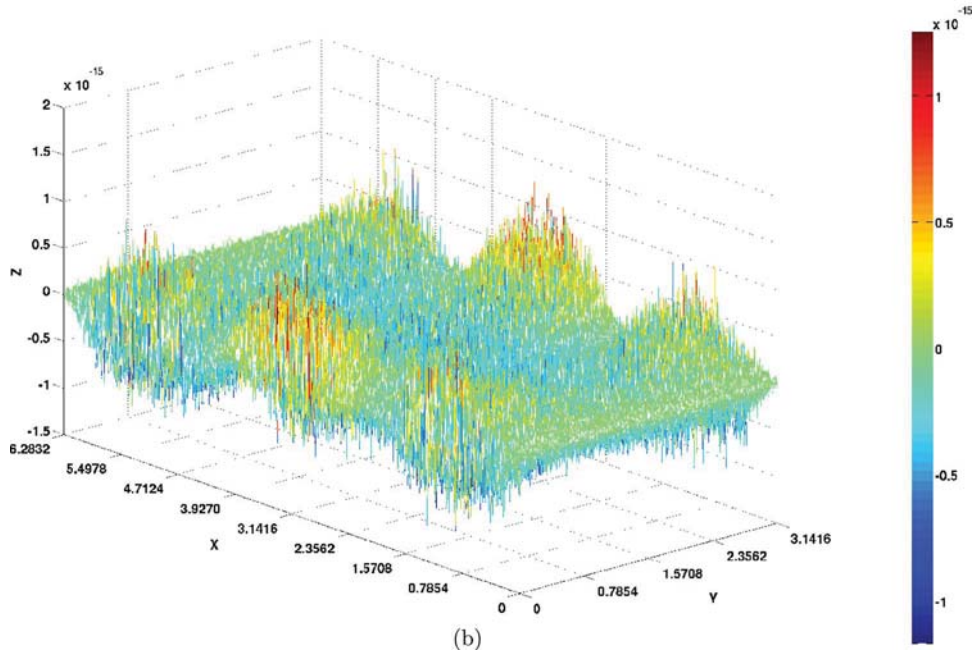

(b)

FIG. 4. As Figure 3 using Taylor's method.

Due to the problems mentioned both methods globally fail the third assessment criterion. Nevertheless, it is worth to mention that the Proudman-Rao method is faster in convergence of the eigenfrequencies, whereas convergence of the velocity field of Taylor's method is high in the interior of the domain, but quite slow at the boundaries. Finally, if one of these two semi-analytical solutions has to be chosen, it remains which property is preferred: satisfaction of boundary conditions (Proudman-Rao method) or satisfaction of governing equations (Taylor's method) up to machine precision.

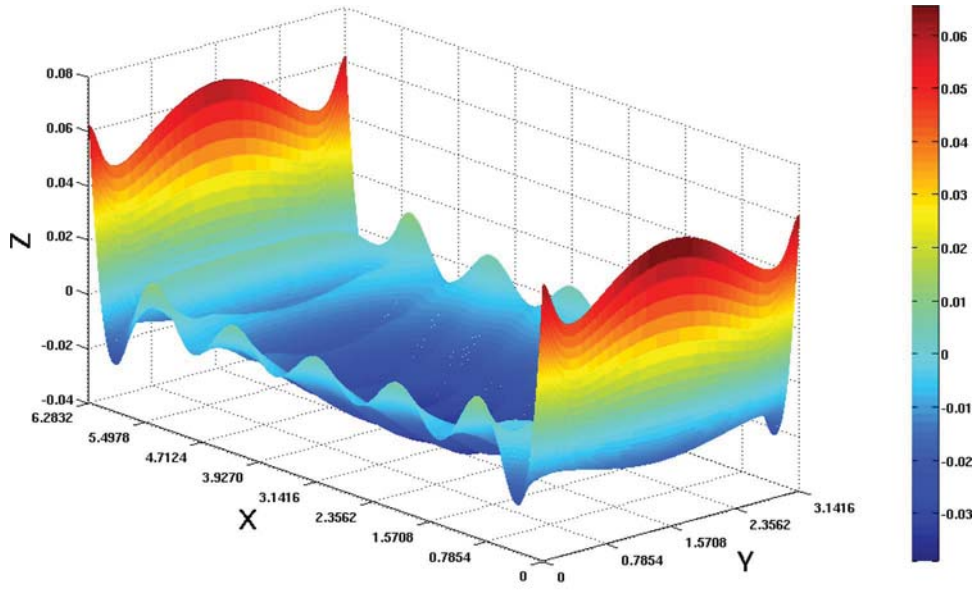

(a)

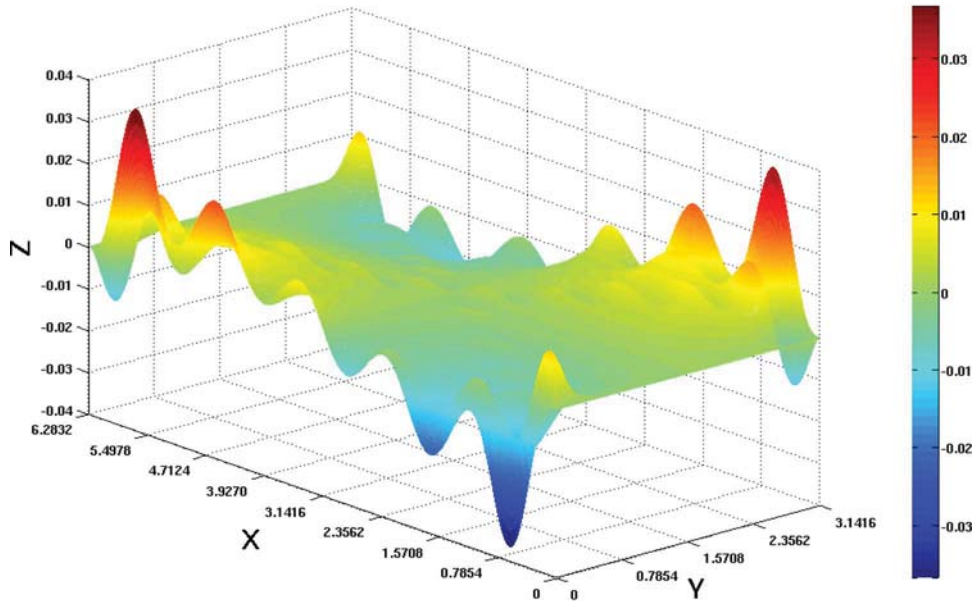

(b)

FIG. 5. Antisymmetric horizontal velocity fields in the x–y plane for a mode with frequency sigma $\sigma \approx 0.657$ are constructed with two alternative algorithms. (a) and (b) subfigures give the differences between the results produced by the Proudman-Rao and Taylor's methods for the u and v velocity components, respectively.

III. FEM SOLUTION OF LINEAR INERTIAL WAVES

In Sec. II, it was shown that both semi-analytical solutions for linear inertial waves have at least one major disadvantage. Therefore, next we present a purely numerical FEM solution for the inertial wave problem. First, the same vertical standing mode decomposition is considered to reduce the inertial wave problem from 3D to 2D. Second, a FEM discretisation of the 2D boundary value

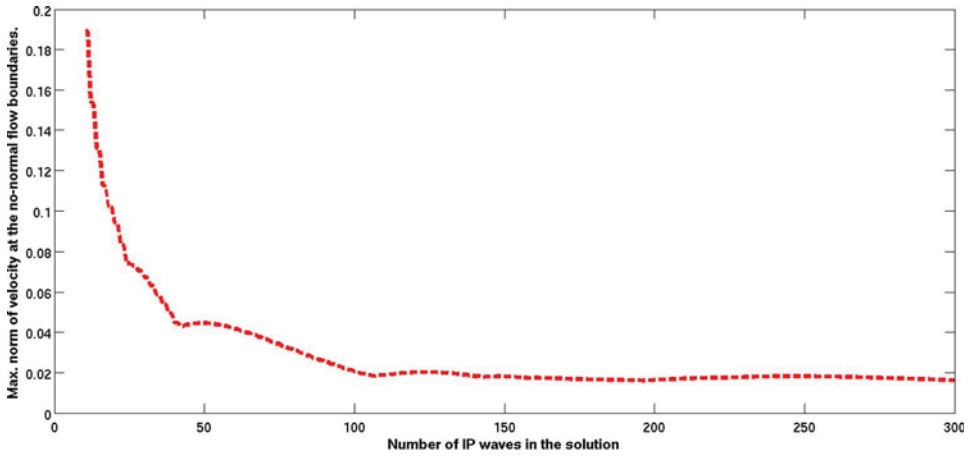

FIG. 6. The maximum (numerical) speed v normal to the East-West boundaries is plotted against the number of IP waves used in Taylor's method.

problem given by the system (4) is constructed, with the mandatory satisfaction of the no-normal flow boundary conditions in a weak sense.

A. Weak formulation and resulting eigenvalue problem

The 2D boundary value problem is given on a rectangular domain $\Omega = \{0 \le x \le L;\ -Y \le y \le Y\}$ by the following partial differential equations:

$$\frac{\partial u}{\partial t} - v = -\partial_x p, \tag{25a}$$

$$\frac{\partial v}{\partial t} + u = -\partial_y p, \tag{25b}$$

$$-q + \partial_x u + \partial_y v = 0, \tag{25c}$$

$$\frac{\partial q}{\partial t} = -p \tag{25d}$$

and no-flow boundary conditions at the walls $\partial\Omega = \cup\Gamma_i$.

The latter system is derived from (4), when the pressure is taken to be $p = \partial^2\zeta/\partial t^2$. The system introduced above is energy conserving, where the energy functional is given by

$$\mathcal{H} = \frac{1}{2}\int_\Omega (u^2 + v^2 + q^2)\, d\Omega. \tag{26}$$

Multiplication of (25) with u, v, p, and q, respectively, integration over the domain followed by a summation and use of the boundary condition $\mathbf{u} \cdot \mathbf{n} = 0$ with outward normal $\mathbf{n}$, results in energy conservation of the system: $\dot{\mathcal{H}} \equiv d\mathcal{H}/dt = 0$, where the dot represents a time derivative.

A weak formulation of (25) is given by

$$\int_\Omega \left(\frac{\partial \mathbf{u}}{\partial t} + \mathbf{u}^\perp\right)\phi\, d\Omega = -\int_\Omega (\nabla p)\phi\, d\Omega, \tag{27a}$$

$$\int_\Omega (-q)\phi\, d\Omega - \int_\Omega \nabla\phi \cdot \mathbf{u}\, d\Omega = -\int_{\partial\Omega} \mathbf{u}\cdot\mathbf{n}\phi\, \mathbf{dS}, \tag{27b}$$

$$\int_\Omega \frac{\partial q}{\partial t}\phi\, d\Omega = -\int_\Omega p\phi\, d\Omega, \tag{27c}$$

where the velocity field is given in terms of the two-dimensional vector $\mathbf{u} = (u, v)^T$, the perpendicular velocity vector is $\mathbf{u}^\perp = (-v, u)^T$, the two-dimensional differential operator is $\nabla = (\partial/\partial x, \partial/\partial y)^T$ and ϕ is a test function taken from $H_0^1(\Omega)$. Hence, the function spaces are chosen to be

$$H_0^1(\Omega) = \{v \in H^1(\Omega) : v = 0 \text{ on } \partial\Omega\}, \text{ with} \tag{28a}$$

$$H^1(\Omega) = \{v \in L^2(\Omega) : \frac{\partial v}{\partial x}, \frac{\partial v}{\partial y} \in L^2(\Omega)\}, \tag{28b}$$

where L^2 is a space of square integrable functions.

Note that after multiplication with a test function ϕ, we only do integration by parts in the continuity equation, and skip the integration by parts in the momentum equation, which is a slight modification of a classical FEM weak formulation. This way we ensure the conservation of the energy on the discrete level, as shown later. The latter is crucial for an accurate and robust numerical scheme.

After taking into an account no flow boundary conditions $\mathbf{u} \cdot \mathbf{n} = \mathbf{0}$ at $\partial\Omega$, (27) becomes

$$\int_\Omega \left(\frac{\partial \mathbf{u}}{\partial t} + \mathbf{u}^\perp\right)\phi \, d\Omega = -\int_\Omega (\nabla p)\phi \, d\Omega, \tag{29a}$$

$$\int_\Omega (-q)\phi \, d\Omega - \int_\Omega \nabla\phi \cdot \mathbf{u} \, d\Omega = 0, \tag{29b}$$

$$\int_\Omega \frac{\partial q}{\partial t}\phi \, d\Omega = -\int_\Omega p\phi \, d\Omega. \tag{29c}$$

Given a tessellation $\mathcal{I}_h$ of the domain Ω, we search for a weak solution of system (29) in

$$V_h = \{v : v \text{ is continuous on } \Omega, v|_K \in \mathcal{P}^d(K) \, \forall K \in \mathcal{I}_h\} \subset H^1(\Omega), \tag{30}$$

with $\mathcal{P}^d(K)$ the space of polynomials of at most degree d on $K \in \mathcal{I}_h$, where $d \geq 0$. Variables u, v, p, q are represented via their expansions in terms of basis functions

$$\mathbf{u} = \mathbf{u}_i\phi_i, \quad p = p_i\phi_i, \quad q = q_i\phi_i, \tag{31}$$

where $\phi_i \in V_h$ and $\mathbf{u}_i, p_i, q_i$ are expansion coefficients. We note that, here and hereafter, we use the Einstein convention implying summation over repeated indices. Incorporation of (31) into the weak formulation (29) results in

$$M_{ij}\dot{\mathbf{u}}_j + M_{ij}\mathbf{u}_\mathbf{j}^\perp = -\mathbf{S}_{ij}p_j, \tag{32a}$$

$$M_{ij}q_j + \mathbf{S}_{ji} \cdot \mathbf{u}_j = 0, \tag{32b}$$

$$M_{ij}\dot{q}_j = -M_{ij}p_j, \tag{32c}$$

where $M_{ij} = \int_{\mathcal{I}_h} \phi_i\phi_j \, d\mathbf{x}$, $\mathbf{S}_{ij} = (S_{ij}^x, S_{ij}^y)^T = \int_{\mathcal{I}_h} \phi_i \nabla\phi_j \, d\mathbf{x}$. If we multiply the discrete momentum equation with $\mathbf{u}_i$, the continuity equation with p_i, (32c) with q_i and sum over all nodes, we will obtain the following equation

$$\frac{d}{dt}\left(\frac{1}{2}\left(M_{ij}\mathbf{u}_i \cdot \mathbf{u}_j + M_{ij}q_iq_j\right)\right) = 0, \tag{33}$$

which ensures the conservation of a discrete energy functional in time, in addition to the conservation at the continuous level.

The unknowns p_j and q_j can be eliminated from (32): when a time derivative of (32b) is taken and the results are substituted into (32a) while using (32c), we obtain

$$M_{ij}\dot{u}_j + S_{il}^x M_{lk}^{-1} S_{jk}^x \dot{u}_j + S_{il}^x M_{lk}^{-1} S_{jk}^y \dot{v}_j = M_{ij}v_j, \tag{34a}$$

$$M_{ij}\dot{v}_j + S_{il}^y M_{lk}^{-1} S_{jk}^x \dot{u}_j + S_{il}^y M_{lk}^{-1} S_{jk}^y \dot{v}_j = -M_{ij}u_j. \tag{34b}$$

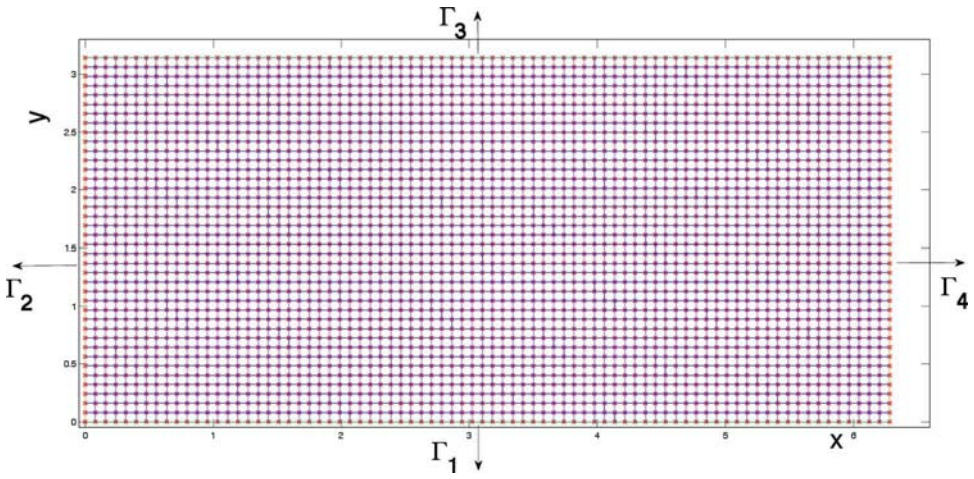

FIG. 7. Tessellation $\mathcal{I}_h$ of the domain Ω with its four boundaries $\Gamma_1, \ldots, \Gamma_4$.

After incorporation of the ansatz $(u, v) \propto \exp(-i\sigma t)$ into (34), we arrive at the following global generalised eigenvalue problem

$$i\sigma \begin{bmatrix} M_{ij} + S^x_{il} M^{-1}_{lk} S^x_{jk} & S^x_{il} M^{-1}_{lk} S^y_{jk} \\ S^y_{il} M^{-1}_{lk} S^y_{jk} & M_{ij} + S^y_{il} M^{-1}_{lk} S^x_{jk} \end{bmatrix} \begin{bmatrix} u_j \\ v_j \end{bmatrix} = \begin{bmatrix} 0 & -M_{ij} \\ M_{ij} & 0 \end{bmatrix} \begin{bmatrix} u_j \\ v_j \end{bmatrix}. \tag{35}$$

B. Numerical eigenfrequencies and tests against semi-analytical solutions

In this section, a numerical solution of the generalised eigenvalue problem (35) is discussed. For the particular simulation two-dimensional linear Bernstein polynomials were chosen as a set of basis functions for the FEM problem given on the rectangular tessellation $\mathcal{I}_h$ of the continuous domain Ω, see Figure 7.

For a given $n \in \mathbb{N}/\{0\}$, the corresponding Bernstein polynomials of degree n are defined by

$$B^n_k(x) = \binom{n}{k} x^k (1-x)^{n-k}, \ \forall x \in [0, 1], \qquad k = 0, 1, ..., n, \tag{36}$$

where $\binom{n}{k}$ is a binomial coefficient and $\mathbb{N}$ is the set of natural numbers. Bernstein polynomials are linearly independent and span the space of polynomials of degree n. Bernstein polynomials are invariant under affine transformations, and all the terms of the Bernstein basis are positive on the interval where they are defined, and their sum equals to one. Additionally, a Bernstein polynomial is always better conditioned than a polynomial of power form for the determination of simple roots on the unit interval [0, 1]. The latter properties justify our choice of Bernstein polynomials to represent the polynomial space in the definition of V_h in (30).

The solution of the generalised eigenvalue problem (35) emerges in pairs of eigenvalues and corresponding eigenvectors. The set of eigenvalues is compared to the eigenvalues calculated from the semi-analytical solutions of the same problem, as discussed in Sec. II. Unfortunately, alongside the acceptable eigenvalues, the method produces high frequency noise. Nevertheless, it appears that numerical, "noisy" eigenvalues are not consistent for different runs, with different mesh sizes, which enable us to construct a simple algorithm for identifying the acceptable eigenvalues from the numerical noise. The numerical implementation of (35) is initialised consequently with four different meshes, four different tessellations of a domain $\Omega = [2\pi \times \pi]$ into 20×10, 40×20, 80×40, and 160×80 elements. The latter results in four sets of eigenvalues. From these four sets of eigenvalues, we notice that acceptable eigenvalues are converging. By contrast, the numerical noise eigenvalues are appearing and disappearing in the different runs. The latter suggests a simple

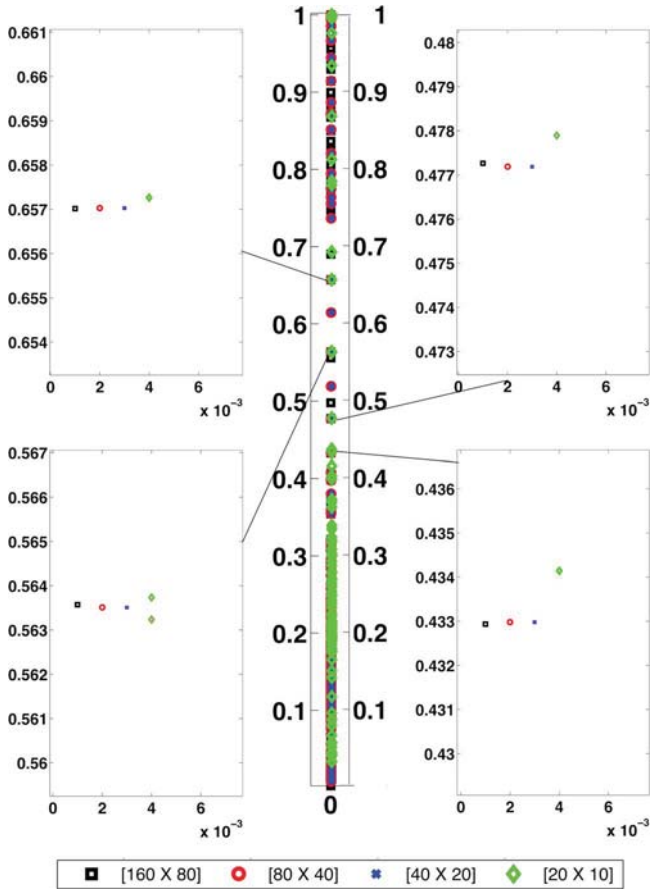

FIG. 8. Four different sets of eigenvalues are plotted here. Black squares, red circles, blue crosses, and green diamonds correspond to the set of eigenvalues from simulations with mesh-sizes 160×80, 80×40, 40×20, and 20×10, respectively. The first four highest eigenfrequencies are highlighted.

"decision algorithm": stationary (one has to allow convergence shifts, of course) eigenvalues for different runs and mesh-size are considered acceptable, and the rest is numerical noise. In other words, in the scale, which corresponds to the densest mesh size, the presence of four converging eigenvalues (from different sets) is identifying the numerical eigenvalue as acceptable, otherwise it is considered numerical noise. In Figure 8, we present a graphical interpretation of the suggested "decision algorithm." The spots that are overlaid from all four sets of eigenvalues on the densest mesh scale ($\Delta x \approx 0.006$) are acceptable. We note that eigenvalues which are close and/or converge to 1 can be neglected, because the eigenfrequency we search for needs to be smaller than one. Also, substantial numerical noise is noticeable near 0, but this behaviour is expected for any solution of a numerical eigenvalue problem. Thus, following the latter "decision algorithm," we are able to reproduce every eigenfrequency found by the semi-analytical methods.

After the exact matching of numerical eigenfrequencies with semi-analytical eigenfrequencies, we proceed to compare the corresponding velocity fields, through the comparison of the eigenvectors. In Sec. II C, the discussion revolved around the comparison of two semi-analytical solutions for the velocity field of the highest eigenfrequency in a $[2\pi \times \pi]$ domain. Hence, here too, we consider the velocity field corresponding to the same $\sigma \approx 0.657$ eigenfrequency. In Figure 9, both components of the numerical two-dimensional velocity field corresponding to the eigenvalue $\sigma \approx 0.657$ are depicted. The numerical velocity field is a result of a simulation on a mesh with 80×40 elements. Flow near the normal boundaries is nearly absent. It is apparent that the equations and the corresponding boundary conditions are satisfied up to FEM accuracy.

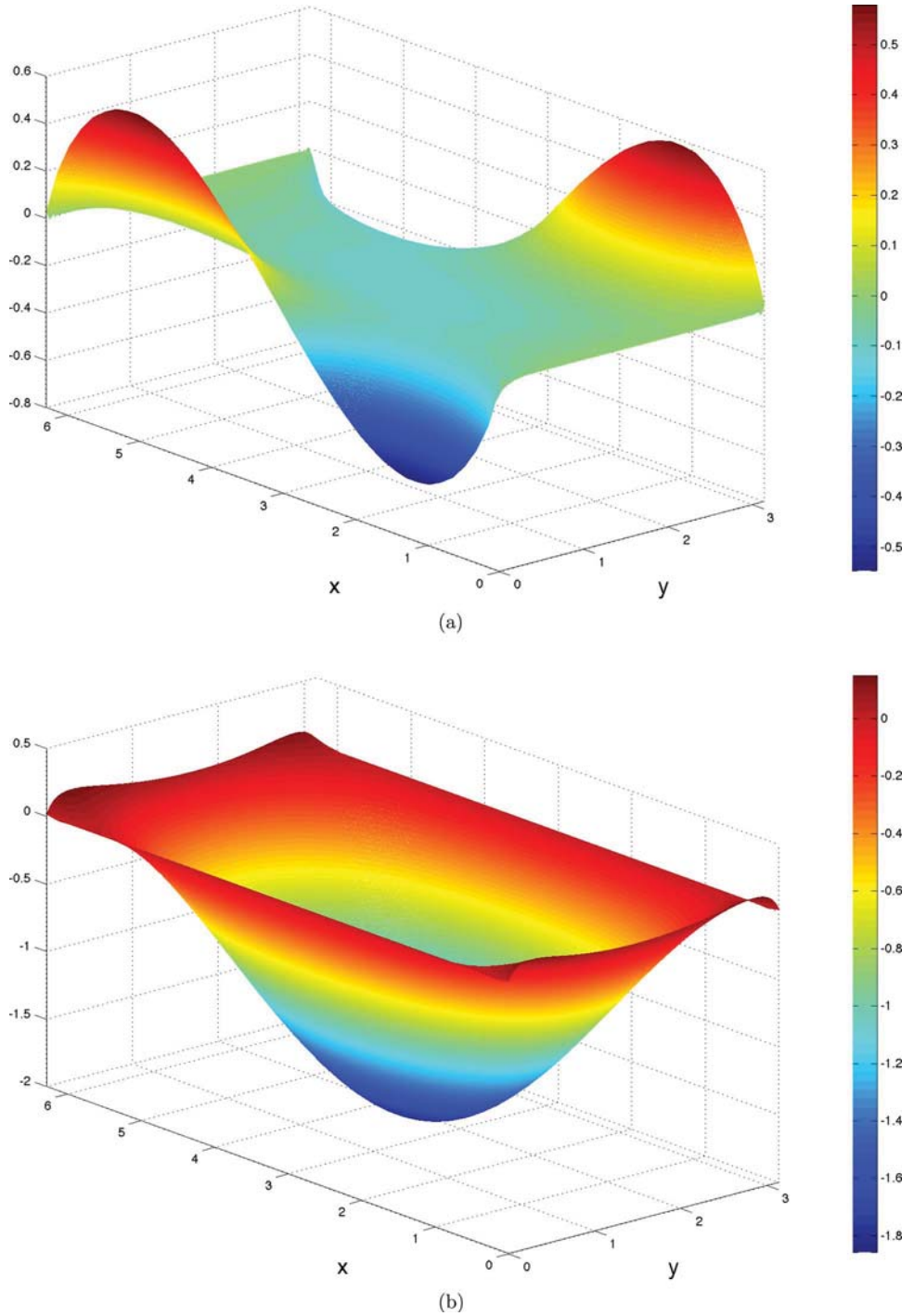

FIG. 9. u and v components of the numerical horizontal velocity for mode $\sigma \approx 0.657$ are presented in (a) and (b) subplots, respectively. An 80×40-element mesh is used for the simulations in a domain which is rotating anti-clockwise. (a) u profile; (b) v profile.

Results discussed in the previous section justify a comparison plot of the numerical solution against just Taylor's semi-analytical solution. Hence, in Figure 10 we introduce a comparison plot of the two velocity vectors. The comparison is fair, due to the comparability in sizes of the resulting eigenvalue problems in both the numerical and semi-analytical cases. As was expected, the difference is noticeable near the normal boundaries, where Taylor's method has slow convergence.

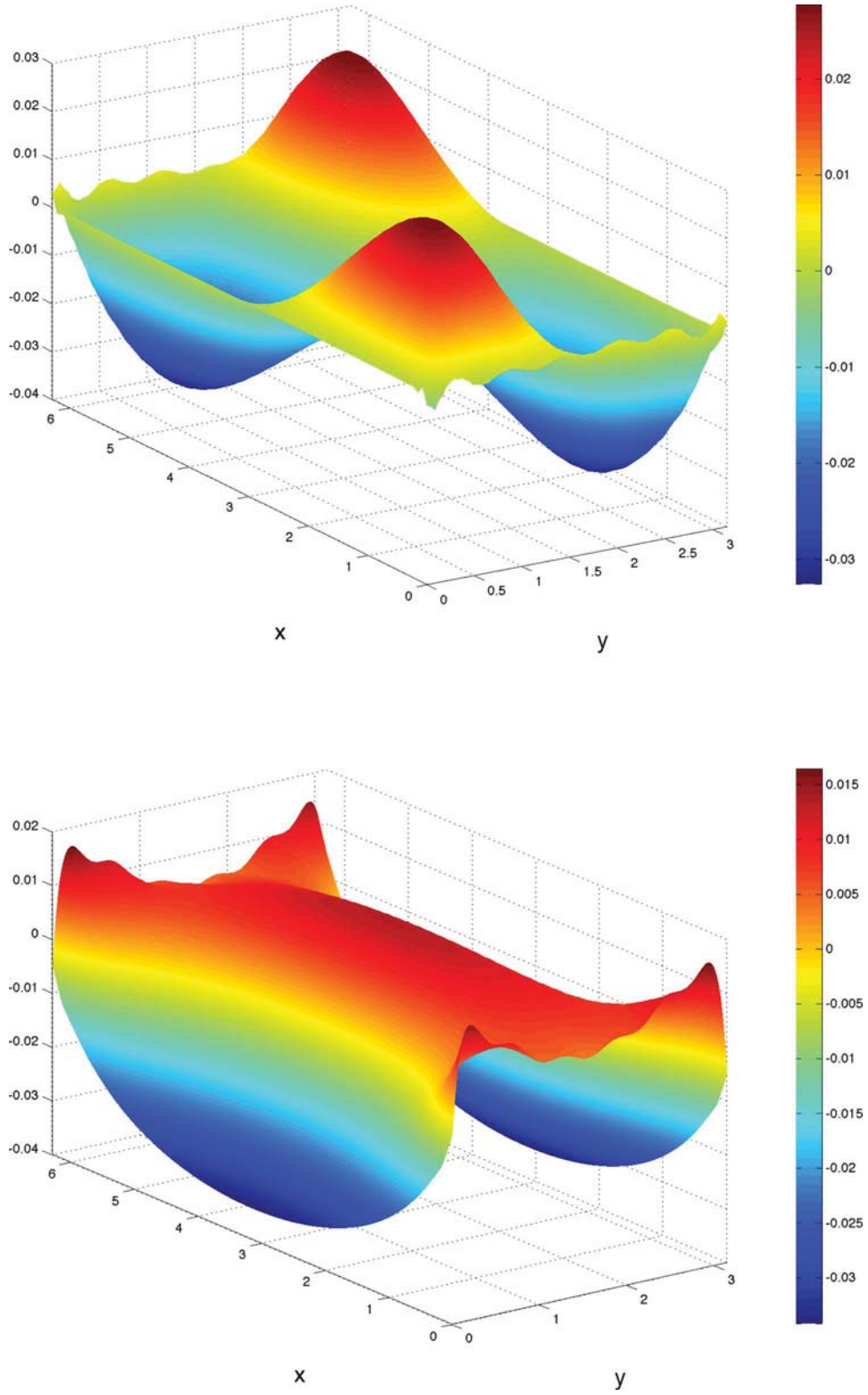

FIG. 10. (a) and (b) subfigures give the difference between the numerical FEM solution and Taylor's semi-analytical solution in the u and v velocity components, respectively. An 80×40-element mesh is used for the FEM simulation.

IV. SUMMARY AND CONCLUSIONS

We have shown numerically that the Proudman-Rao method for deriving modal solutions of the linear, rotating incompressible Euler equations in a (planar) rectangular parallelepiped bounded with solid walls suffers from poor convergence in the interior of the fluid domain as well as a Gibbs phenomenon at the boundaries. Despite the concise structural construction, the solution is practically unusable. Therefore, an alternative mode decomposition solution (Taylor's method) was presented. The three-dimensional problem was reduced to a two-dimensional problem by using the ansatz of vertical modes in the z-direction, exactly repeating the arguments from Maas.[8] By scaling the depth of the tank with $H_*/n\pi$ for the vertical mode n, we remove all references to the vertical and the problem can be solved for each vertical mode strictly in the horizontal plane (whose size is fixed except for an n-dependent rescaling of the basin's size). The resulting two-dimensional problem in the horizontal plane was solved by employing ideas and results that Taylor[1] used to determine the rotational effects on long surface gravity waves. As in the Proudman-Rao method, Taylor's method also leads to an infinite matrix eigenvalue problem, whose solution upon truncation gives similar results. The novel mode solutions satisfy the linear Euler equations exactly, thus they are considered to be an improvement over those obtained with the Proudman-Rao method. Nevertheless, the novel semi-analytical solution has its own flaws. The mode solutions are, by construction, a superposition of inertial analogs of surface Kelvin and Poincaré wave solutions, which converge to solutions that satisfy the solid-wall boundary conditions. Unfortunately, the latter convergence is also slow. By contrast, the Proudman-Rao solution satisfies the no-normal flow boundary conditions exactly.

The latter motivated us to apply a continuous FEM discretisation to the reduced two-dimensional problem (based on using a standing wave in the vertical of the original three-dimensional problem) in order to obtain numerical mode solutions that (weakly) satisfy no-normal flow boundary conditions by construction. A modified FEM discretisation is proven to be symmetric and energy conserving on a discrete level, which plays an essential role in the stability and accuracy of this scheme (e.g., Bokhove and Johnson[25]). The resulting discrete system is solved via a generalised eigenvalue solver, which unfortunately produces a substantial amount of numerical noise. Nevertheless, a simple "decision algorithm" is suggested to separate acceptable numerical eigenfrequencies from numerical noise. Finally, this numerical solution is tested against the semi-analytical solution.

Extensive comparison between the two semi-analytical and numerical solutions enables one to adopt the most appropriate method for resolving the inertial waves. The Proudman-Rao method facilitates fast convergence of eigenfrequencies and the determination of semi-analytical solutions that satisfy the boundary conditions exactly because this is embedded in the construction algorithm. However, this method displays a Gibbs phenomenon at the boundaries. Unlike the Proudman-Rao method, Taylor's method enables a semi-analytical solution exactly satisfying the governing equations in the interior, but with slow convergence near the boundaries. The numerical solution, based on a modified FEM discretisation, implements a very accurate but relatively slow method, which requires an extra step to separate the acceptable eigenfrequencies from numerical noise. Depending on one's needs one might choose one of the suggested methods.

The solutions we have presented have been used to verify the novel numerical technique developed in Nurijanyan *et al.*[26] for the initial-value problem of three-dimensional inertial waves in arbitrarily shaped domains. This method is geared to investigate whether wave attractors (Maas,[9] Manders and Maas,[23] and Rieutord *et al.*[27]) and complex eigenmodes (such as in Bokhove and Ambati[28]) emerge in domain shapes of sufficient geometric complexity.

Additionally, we note that solutions of the Euler equations, by default inviscid, presented above are also relevant in the viscous case (Navier-Stokes equations), which is not intuitive at first glance. In experiments like those in Fultz,[10] McEwan,[11] Manasseh,[12,13] Kobine,[14] Thompson,[15] Aldridge and Toomre,[16] Malkus,[17] Vanyo *et al.*,[18] Beardsley,[19] Bewley *et al.*,[20] Lamriben *et al.*,[21] Boisson *et al.*,[22] and Manders and Maas,[23] a variety of forcing mechanisms and geometries have been applied. In some cases forcing occurs by pumping through viscous boundary layers, e.g., either on convex (outer) or concave (inner) parts of spherical shells; in other studies by means of the Euler force (using libration). Experiments performed in square domains (Bewley *et al.*,[20] Lamriben *et al.*,[21] and Boisson *et al.*[22]) seem to show that inviscid eigenmodes derived above are relevant in the sense that

energy spectra display peaks at inviscid eigenfrequencies of some of the larger scale eigenmodes. In two experiments (Bewley *et al.*[20] and Lamriben *et al.*[21]) forcing arises by pulling a grid through the fluid, leaving a set of waves behind. In another experiment with a libration (Boisson *et al.*[22]), forcing occurs through Ekman-layer convergence, lending the spatial structure of the response much more of a beam-like character. Note, however, that due to the degeneracy discussed in Maas[8] (near-degeneracy for numerical results) internal (gravity) and inertial waves have a much more flexible ("chameleonic") spatial structure than that of the eigenmodes of elliptic problems (like surface waves). Indeed, in general one observes that the inviscid response (in combination with any spatial structure in the forcing) is determining the field's spatial structure, slaving the viscous (boundary layer) response, and not the other way around.

ACKNOWLEDGMENTS

We would like to acknowledge the financial support of the Netherlands Foundation for Technical Research (STW) for the project "A numerical wave tank for complex wave and current interactions."

[1] G. I. Taylor, "Tidal oscillations in gulfs and rectangular basins," Proc. London Math. Soc. **20**, 148–181 (1922).
[2] Lord Rayleigh, "Notes concerning tidal oscillations upon a rotating globe," Proc. R. Soc. London **82**(556), 448–464 (1909), http://www.jstor.org/stable/92854.
[3] J. Proudman, "On the dynamic equation of the tides. Parts 1–3," Proc. London Math. Soc., Ser. 2 **18**, 1–68 (1917).
[4] J. Proudman, "Note on the free tidal oscillations of a sea with slow rotation," Proc. London Math. Soc. **s2-35**, 75–82 (1933).
[5] P. H. LeBlond and L. A. Mysak, *Waves in the Ocean* (Elsevier, Amsterdam, 1978).
[6] L. Kelvin, "Vibrations of a columnar vortex," Philos. Mag. **10**, 155–168 (1880).
[7] G. H. Bryan, "The waves on a rotating liquid spheroid of finite ellipticity," Philos. Trans. R. Soc. London, Ser. A **180**, 187–219 (1889).
[8] L. R. M. Maas, "On the amphidromic structure of inertial waves in a rectangular parallelepiped," Fluid Dyn. Res. **33**, 373–401 (2003).
[9] L. R. M. Maas, "Wave focussing and ensuing mean flow due to symmetry breaking in rotating fluids," J. Fluid Mech. **437**, 13–28 (2001).
[10] D. Fultz, "A note on overstability and the elastoid-inertia oscillations of Kelvin, Solberg and Bjerknes," J. Meteorol. **16**, 199–208 (1959).
[11] A. D. McEwan, "Inertial oscillations in a rotating fluid cylinder," J. Fluid Mech. **40**, 603–640 (1970).
[12] R. Manasseh, "Breakdown regimes of inertia waves in a precessing cylinder," J. Fluid Mech. **243**, 261–296 (1992).
[13] R. Manasseh, "Distortions of inertia waves in a rotating fluid cylinder forced near its fundamental mode resonance," J. Fluid Mech. **265**, 345–370 (1994).
[14] J. J. Kobine, "Inertial wave dynamics in a rotating and precessing cylinder," J. Fluid Mech. **303**, 233–252 (1995).
[15] R. O. R. Y. Thompson, "A mechanism for angular momentum mixing," Geophys. Astrophys. Fluid Dyn. **12**, 221–234 (1979).
[16] K. D. Aldridge and A. Toomre, "Axisymmetric oscillations of a fluid in a rotating spherical container," J. Fluid Mech. **37**, 307–323 (1969).
[17] W. V. R. Malkus, "Precession of the earth as the cause of geomagnetism," Science **160**, 259–264 (1968).
[18] J. Vanyo, P. Wilde, P. Cardin, and P. Olson, "Experiments on precessing flows in the earth's liquid core," Geophys. J. Int. **121**, 136–142 (1995).
[19] R. C. Beardsley, "An experimental study of inertial waves in a closed cone," Stud. Appl. Math. **49**, 187–196 (1970).
[20] G. P. Bewley, D. P. Lathrop, L. R. M. Maas, and K. R. Sreenivasan, "Inertial waves in rotating grid turbulence," Phys. Fluids **19**, 071701 (2007).
[21] C. Lamriben, P. P. Cortet, F. Moisy, and L. R. M. Maas, "Excitation of inertial modes in a closed grid turbulence experiment under rotation," Phys. Fluids **23**, 015102 (2011).
[22] J. Boisson, C. Lamriben, L. R. M. Maas, P. Cortet, and F. Moisy, "Inertial waves in rotating grid turbulence," Phys. Fluids **24**, 076602 (2012).
[23] A. M. M. Manders and L. R. M. Maas, "Observations of inertial waves in a rectangular basin with one sloping boundary," J. Fluid Mech. **493**, 59–88 (2003).
[24] D. Rao, "Free gravitational oscillations in rotating rectangular basins," J. Fluid Mech. **25**, 523–555 (1966).
[25] O. Bokhove and E. Johnson, "Hybrid coastal and interior modes for two-dimensional flow in a cylindrical ocean," J. Phys. Oceanogr. **29**, 93–118 (1999).
[26] S. Nurijanyan, J. van der Vegt, and O. Bokhove, "Hamiltonian discontinuous Galerkin FEM for linear, rotating incompressible Euler equations: Inertial waves," J. Comput. Phys. **241**, 502–525 (2013).
[27] M. Rieutord, B. Georgeot, and L. Valdettaro, "Inertial waves in a rotating spherical shell: attractors and asymptotic spectrum," J. Fluid Mech. **435**, 103–144 (2001).
[28] O. Bokhove and V. R. Ambati, "Hybrid Rossby-shelf modes in a laboratory ocean," J. Phys. Oceanogr. **39**(10), 2523–2542 (2009).